Geochemistry Geophysics Geosystems G3

Article
Volume 11, Number 8
5 August 2010
Q08006, doi:10.1029/2010GC003130
ISSN: 1525-2027

Published by AGU and the Geochemical Society

An analytical benchmark with combined pressure and shear loading for elastoplastic numerical models

V. M. Yarushina, M. Dabrowski, and Y. Y. Podladchikov

Physics of Geological Processes, University of Oslo, PB 1048 Blindern, N-0316 Oslo, Norway (v.m.yarushina@matnat.uio.no)

[1] We discuss the benchmark strategy to check the accuracy of elastoplastic numerical solutions based on a fully two-dimensional analytical solution. Associated rate-independent non-hardening plasticity with von Mises or Tresca criteria is assumed throughout. Algorithms for integration of the rate equations, strategies for stress updating over a time step, and tangent operators are discussed. The accuracy of a simple incremental algorithm as a function of the time step is discussed.

Components: 6000 words, 9 figures.

Keywords: elastoplasticity; numerical modeling; analytical solutions; finite elements.

Index Terms: 1906 Informatics: Computational models, algorithms; 0545 Computational Geophysics: Modeling (1952, 4255); 3225 Mathematical Geophysics: Numerical approximations and analysis (4260).

Received 16 March 2010; **Revised** 14 June 2010; **Accepted** 18 June 2010; **Published** 5 August 2010.

Yarushina, V. M., M. Dabrowski, and Y. Y. Podladchikov (2010), An analytical benchmark with combined pressure and shear loading for elastoplastic numerical models, *Geochem. Geophys. Geosyst.*, *11*, Q08006, doi:10.1029/2010GC003130.

1. Introduction

[2] An overwhelming majority of natural and engineering materials exhibit elastoplastic or viscoplastic properties either at ambient or elevated temperatures. Plasticity is important in metal forming processes, in estimation of a collapse load and a permissible working stress in metal and composite engineering structures. Soils and rocks carrying the structure have to be able to support its weight without visible failure. Pore collapse in ductile porous materials and formation of shear bands indicate plastic behavior in rocks.

[3] Because of the complexity of boundary conditions and the nonlinearity of the processes considered within the elastoplastic analysis, general solutions of the mathematical equations rely on numerical approximations. Today the finite element method is the most widely used tool in the prediction of both linear and nonlinear structural behavior. However, an inherent danger of such widespread use is overconfidence in the accuracy and correctness of the results obtained, although numerical aspects may play an important role. Because plasticity theory assumes infinitesimal increments, it is almost inevitable that solution procedures using discrete load steps will lead to some error. The accuracy of numerical solutions can be tested in several ways. The usual strategy is to compare numerical results either with analytical solutions for given simplified initial and boundary conditions, experimental data, or with reference numerical solutions [*Krieg and Krieg*, 1977; *Ortiz and Popov*, 1985; *Simo and Hughes*, 1998; *Roberts et al.*, 1992; *Wieners*, 1999]. In linear elastic problems it is relatively

straightforward to find exact solutions to which the finite element results may be compared. In nonlinear elastoplastic analyses it is much more difficult to determine suitable benchmarks. However, in these cases it is even more important to establish a set of benchmarks to which quantitative or qualitative comparisons may be made.

[4] One of the popular 2D elastoplastic benchmark examples is isotropic contraction (expansion) of the circular plate with a circular hole under plane strain to which an analytical solution of *Hill* [1950] can be applied. However, this solution does not involve shear deformation and a reference numerical solution for the rectangle with a hole stretched in one direction under plane strain or under pure shear is often used to check the accuracy for non-hydrostatic loading [*Barthold et al.*, 1998; *Krabbenhoft et al.*, 2007]. In this paper we discuss a benchmark test for an elastoplastic plate with a circular hole under combined pressure and shear loads based on Galin's analytical solution [*Galin*, 1946]. This benchmark is suitable for both compressible materials with Tresca type of plasticity and incompressible materials obeying either Tresca or von Mises yield criteria.

[5] Techniques for solving the global equations associated with nonlinear finite element analysis can be classified broadly as either iterative or incremental. The accuracy of simple incremental schemes as well as the efficiency and stability of some classical iterative schemes are strongly influenced by the load increment size. Here, we evaluate four numerical models, including the very simple incremental forward Euler, modified Newton-Raphson with consistent and continuum tangent modular matrixes and the Picard iteration method.

2. Rate-Independent Elastoplasticity: Constitutive Relations

[6] Both the numerical and analytical modeling in this paper are based on the classical flow theory for small elastoplastic deformations which is presented in a number of monographs and textbooks [*Hill*, 1950; *Kachanov*, 1971; *Davis and Selvadurai*, 2002; *Yu*, 2006]. This theory assumes the additive decomposition of the total strain tensor e into elastic strain e^e and plastic strain e^p

$$e = e^e + e^p \quad (e_{ij} = e^e_{ij} + e^p_{ij}) \tag{1}$$

Or in the rate form:

$$\dot{e} = \dot{e}^e + \dot{e}^p \quad (\dot{e}_{ij} = \dot{e}^e_{ij} + \dot{e}^p_{ij}) \tag{2}$$

The elastic strain determines the Cauchy stress tensor σ through Hooke's law:

$$\sigma = De^e \quad (\sigma_{ij} = D_{ijkl}e^e_{kl}) \tag{3}$$

In the rate form:

$$\dot{\sigma} = D\dot{e}^e \quad (\dot{\sigma}_{ij} = D_{ijkl}\dot{e}^e_{kl}) \tag{4}$$

where D is the elastic stiffness tensor. In contrast, there is no unique correspondence between plastic strain and stress. Applied stress controls only plastic strain increments that can be written in the form of the plastic flow rule:

$$\dot{e}^p = \dot{\lambda}\frac{\partial Q}{\partial \sigma} \quad \left(\dot{e}^p_{ij} = \dot{\lambda}\frac{\partial Q}{\partial \sigma_{ij}}\right) \tag{5}$$

where λ is the positive plastic multiplier and $Q = Q(\sigma_{ij})$ is the plastic potential. A dot denotes the time derivative. It is essential that plastic yielding occurs only when stresses reach the certain yield surface $F = 0$ and remain on it (this would imply $dF = 0$). When stresses move inside the yield surface, elastic unloading begins, during which plastic strains remain constant so that $\dot{\lambda} = 0$. Therefore unloading refers to an element that passes from a plastic state to an elastic state. In the absence of hardening (perfect plasticity) yield function depends only on stress components $F = F(\sigma_{ij})$. Conditions of plastic loading or elastic unloading, i.e., consistency conditions, can be written as follows [e.g., *Kachanov*, 1971; *Yu*, 2006]:

$$\begin{aligned} &\textit{elastic}: && \dot{\lambda} = 0 && \textit{if} && F(\sigma) < 0 \\ &\textit{unloading}: && \dot{\lambda} = 0 && \textit{if} && F(\sigma) = 0,\ dF = \frac{\partial F}{\partial \sigma}d\sigma < 0 \\ &\textit{loading}: && \dot{\lambda} > 0 && \textit{if} && F(\sigma) = 0,\ dF = \frac{\partial F}{\partial \sigma}d\sigma = 0 \end{aligned} \tag{6}$$

The plastic flow rule (5) implies that principal axes of plastic strain rates and stresses are coincident [*Chakrabarty*, 2006, p. 75]. However, in some geological materials such as soils, these principal axes are not always parallel. In this case special non-coaxial models such as that of *Rudnicki and Rice* [1975] have to be considered. When yield function is used as a plastic potential, i.e., $Q(\sigma_{ij}) = F(\sigma_{ij})$, one can speak about the associated flow rule. In this case, the strain rate vector is normal to the yield surface. The exceptions are singular points of non-smooth yield surfaces (such as edges of Tresca prism or Mohr-Coulomb cone) where the flow vector takes any intermediate direction lying within the angle formed by the normals to the two adjacent faces.

[7] Note that by using the plastic flow rule (5), the incremental form of equations (2), (4) and the

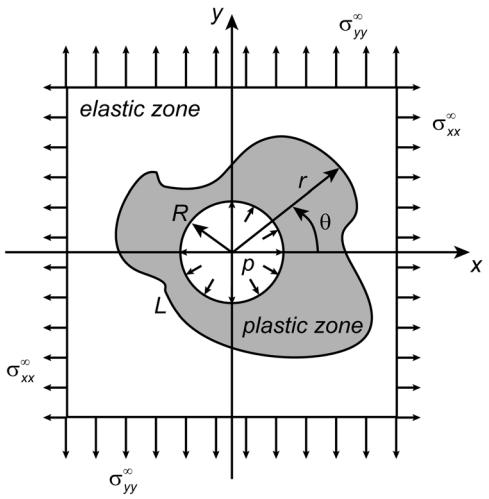

Figure 1. Setup of the problem with the elastoplastic extension (compression) of a plane with a circular hole. Two different homogeneous forces applied at the remote boundary pull the plane in two perpendicular directions. Cartesian and polar coordinates x, y and r, θ originate at the hole center. The hole boundary with radius R is subjected to the uniform pressure p. A plastic zone of unknown geometry develops around the hole. The boundary conditions at the hole are: $\sigma_{rr}|_{r=R} = -p(t)$, $\sigma_{r\theta}|_{r=R} = 0$, at the remote boundary $\sigma_{xx} \to \sigma^{\infty}_{xx}(t)$, $\sigma_{yy} \to \sigma^{\infty}_{yy}(t)$, $\sigma_{xy} \to 0$ as $r \to \infty$.

consistency condition for loading $dF = 0$, one can write the complete relationship between total strain rates and stress rates as follows (for derivation see, for example *Davis and Selvadurai* [2002] and *Yu* [2006]):

$$\dot{\sigma} = D^{ep}\dot{e} \tag{7}$$

with elastoplastic stiffness matrix D_{ep} having components

$$D^{ep}_{ijkl} = D_{ijkl} - D_{ijmn}\frac{\partial Q}{\partial \sigma_{mn}}\frac{\partial F}{\partial \sigma_{pq}}D_{pqkl}\left(\frac{\partial F}{\partial \sigma_{rs}}D_{rstv}\frac{\partial Q}{\partial \sigma_{tv}}\right)^{-1} \tag{8}$$

3. Analytical Solution

[8] The analytical solution we use for the numerical code benchmarking was derived by *Galin* [1946] for the elastoplastic extension (compression) of an infinite plate with a circular hole by the combined application of uniform internal pressure p and a couple of forces acting in x, y-directions (Figure 1). The deformation occurs under plane strain conditions. The material obeys the Tresca yield criterion which means that it is plastically incompressible although there can be elastic volume changes. The size and shape of the plastic zone depends on the loading paths and can be determined during the boundary value problem solving. As the external loads are gradually increased from zero, the plate first deforms elastically. Kolossof-Muskhelishvili's method for a plane problem [*Muskhelishvili*, 1953] gives the stress field σ_{ij} of the form

$$\sigma_{xx} + \sigma_{yy} = \sigma_{rr} + \sigma_{\theta\theta} = 4\mathrm{Re}\Phi(z)$$

$$\sigma_{yy} - \sigma_{xx} + 2i\sigma_{xy} = (\sigma_{\theta\theta} - \sigma_{rr} + 2i\sigma_{r\theta})e^{-2\theta i} = 2[\bar{z}\Phi'(z) + \Psi(z)]$$

where $i = \sqrt{-1}$, $z = x + iy = re^{i\theta}$, $\bar{z} = x - iy = re^{-i\theta}$; bar stands for complex conjugate. From the boundary conditions complex potentials are found to be

$$\Phi(z) = \frac{P^{\infty}}{2} + \tau^{\infty}\frac{R^2}{z^2}$$

$$\Psi(z) = \tau^{\infty} + \Delta P\frac{R^2}{z^2} + 3\tau^{\infty}\frac{R^4}{z^4}$$

where $P^{\infty} = -(\sigma^{\infty}_{xx} + \sigma^{\infty}_{yy})/2$ is the far-field pressure, $\tau^{\infty} = (\sigma^{\infty}_{yy} - \sigma^{\infty}_{xx})/2$ is the far-field shear stress, and $\Delta P = P^{\infty} - p$ is the effective pressure. A general solution for the displacements u_x, u_y has the form

$$2\mu(u_x + iu_y) = (3 - 4\nu)\varphi(z) - z\overline{\varphi'(z)} - \overline{\psi(z)}$$

$$\Phi(z) = \varphi'(z), \quad \Psi(z) = \psi'(z)$$

with ν and μ being Poisson's ratio and the elastic shear modulus respectively. Application of boundary conditions gives

$$2\mu(u_x + iu_y) = (1 - 2\nu)P^{\infty}z - \tau^{\infty}R^2\left(\frac{3 - 4\nu}{z} + \frac{z}{\bar{z}^2}\right) - \tau^{\infty}\bar{z} + \Delta P\frac{R^2}{\bar{z}} + \tau^{\infty}\frac{R^4}{\bar{z}^3}$$

This elastic solution is valid until stresses in the plate reach the Tresca yield criterion, which takes the form

$$(\sigma_{xx} - \sigma_{yy})^2\Big/4 + \sigma^2_{xy} = k^2$$

under an assumption that the axial stress $\sigma_{zz} = \nu(\sigma_{xx} + \sigma_{yy})$ is intermediate. In terms of the complex potentials this yield criterion can be reformulated as

$$|\bar{z}\Phi'(z) + \Psi(z)| = k$$

This equation implies that the plate is in the elastic state while the external loads satisfy the condition

$$2|\tau^{\infty}| + |\Delta P| < k$$

[9] If this constraint is violated, two separate plastic zones form originating at opposite points on the hole rim. Here, we do not consider the initial stages of the plastic yielding, although there are analytical solutions that describe this stage of deformation [*Bykovtsev and Tsvetkov*, 1987] based on the perturbation method. We begin our analysis from the point where the plastic zone completely covers the hole. This happens when external loads reach certain threshold values that are discussed in detail in section 3.3. Besides *Galin*'s [1946] original paper, the solution of the problem was discussed in a number of textbooks, such as *Kachanov* [1971] and *Chakrabarty* [2006] where the expansion of incompressible media is studied. Furthermore, we take into account both compressible and incompressible limits in the expansion-contraction problem.

3.1. Plastic Domain

[10] To solve analytically the problem of the elastoplastic plate with a hole, two sets of governing equations need to be considered, one for the plastic zone and another for the elastic domain. In the plastic zone the problem is statically determined, i.e., the stress field is found from the equilibrium equations, yield criterion, and boundary conditions prescribed at the hole rim. It is hypothesized that the radial, hoop, and shear components of stress do not depend on the polar angle θ in the plastic zone since they are constant on the hole rim. The external loads that lead to such a stress state are discussed in section 3.3. If the out of plane stress $\sigma_{zz} = \nu(\sigma_{xx} + \sigma_{yy})$ is intermediate, then the Tresca yield criterion gives

$$F = (\sigma_{rr} - \sigma_{\theta\theta})^2/4 + \sigma_{r\theta}^2 - k^2 = 0 \tag{9}$$

where k is the yield stress in pure shear. Integration of the stress equilibrium equations

$$\frac{\partial \sigma_{rr}}{\partial r} + \frac{\sigma_{rr} - \sigma_{\theta\theta}}{r} = 0, \quad \frac{\partial}{\partial r}\left(r^2 \sigma_{r\theta}\right) = 0$$

together with yield criterion (9) gives the stresses in the plastic zone

$$\sigma_{rr} = -p - 2k\xi \ln(r/R)$$

$$\sigma_{\theta\theta} = -p - 2k\xi(\ln(r/R) + 1)$$

$$\sigma_{r\theta} = 0 \tag{10}$$

where ξ is the sign of the effective pressure ΔP; $\xi = 1$ for compaction and $\xi = -1$ for extension.

[11] Despite the fact that the stress field is axisymmetric in the plastic zone, displacement components u_r and u_θ depend on both spatial coordinates. There is no closed-form analytical solution for the displacement field inside the plastic zone. An approximate solution was found by *Ivlev* [1957] using perturbation theory. The exact solution was derived by *Ostrosablin* [1984] who considered only the case of tensile far-field loading. Here, we use the latter solution to obtain the displacement field in the plastic zone. We also assume that the plastic potential is the same as the yield function, i.e., $Q = F$. In this case plastic flow does not contribute to the volumetric deformation. Therefore, volumetric strain $e_{rr} + e_{\theta\theta}$ even in the plastic region is fully reversible, i.e.

$$e_{rr} + e_{\theta\theta} = \frac{1 - 2\nu}{2\mu}(\sigma_{rr} + \sigma_{\theta\theta}) \tag{11}$$

for associated plasticity shear strain $e_{r\theta} = 0$ due to absence of shear stresses. Expressing strain in terms of displacement components gives two equations for unknown u_r, u_θ in the plastic region

$$\frac{\partial u_r}{\partial r} + \frac{u_r}{r} + \frac{1}{r}\frac{\partial u_\theta}{\partial \theta} = \frac{1 - 2\nu}{2\mu}(\sigma_{rr} + \sigma_{\theta\theta})$$

$$\frac{\partial u_\theta}{\partial r} - \frac{u_\theta}{r} + \frac{1}{r}\frac{\partial u_r}{\partial \theta} = 0 \tag{12}$$

Following *Ostrosablin* [1984] we introduce dimensionless displacement field

$$u_1 = \frac{\mu}{2kc(1 - \nu)}(u_r - u_0), \quad u_2 = \frac{\mu}{2kc(1 - \nu)}u_\theta$$

where

$$c = R \exp\left(-\frac{\Delta P}{2k} - \frac{1}{2}\right)$$

$$u_0 = \frac{1 - 2\nu}{2\mu} r\sigma_{rr} = \frac{1 - 2\nu}{2\mu} r(-p + 2k \ln(r/R))$$

After some algebra, equations (12) yield the well-known equation of telegraphy for both u_1 and u_2. Integration by Riemann's method gives

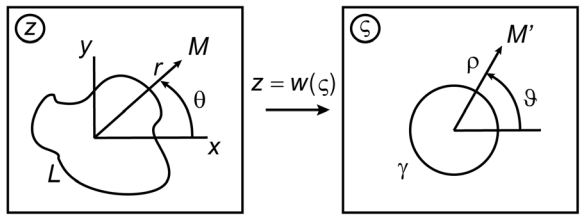

Figure 2. Conformal mapping of the original physical z-plane onto the complex ς-plane allows the setting of the unknown geometry of the elastoplastic boundary.

the displacement field in the plastic region of the form

$$\frac{\mu}{2(1-\nu)kc}u_r = \frac{1-2\nu}{2(1-\nu)}\frac{r}{c}\left(-\frac{p}{2k}+\ln\frac{r}{R}\right)+\frac{1}{2}[f(\theta_1)+f(\theta_2)] + \frac{1}{2}\int_{\theta_1}^{\theta_2}\left\{f(\eta)I_0^*(\lambda(\eta))\left[\ln\frac{c\tilde{r}(\eta)}{r}-(\eta-\theta)\frac{\tilde{r}'(\eta)}{\tilde{r}(\eta)}\right] + I_0(\lambda(\eta))\left[g'(\eta)+f(\eta)-g(\eta)\frac{\tilde{r}'(\eta)}{\tilde{r}(\eta)}\right]\right\}d\eta \tag{13}$$

$$\frac{2\mu}{4kc(1-\nu)}u_\theta = \frac{1}{2}[g(\theta_1)+g(\theta_2)] + \frac{1}{2}\int_{\theta_1}^{\theta_2}\left\{g(\eta)I_0^*(\lambda(\eta))\left[\ln\frac{c\tilde{r}(\eta)}{r}-(\eta-\theta)\frac{\tilde{r}'(\eta)}{\tilde{r}(\eta)}\right] + I_0(\lambda(\eta))\left[f'(\eta)-g(\eta)+f(\eta)\frac{\tilde{r}'(\eta)}{\tilde{r}(\eta)}\right]\right\}d\eta \tag{14}$$

where $I_0(\lambda) = \sum_{n=0}^{\infty}\frac{(\lambda/2)^{2n}}{n!n!}$ is the modified Bessel function of the first kind,

$$I_0^*(\lambda) = \frac{1}{\lambda}\frac{dI_0(\lambda)}{d\lambda}$$

$$\tilde{r}(\eta) = c\frac{1-(\tau^\infty/k)^2}{\sqrt{(\tau^\infty/k)^2-2(\tau^\infty/k)\cos 2\eta+1}}$$

$$\lambda(\eta) = \sqrt{\ln^2\frac{c\tilde{r}(\eta)}{r}-(\eta-\theta)^2}$$

$$f(\eta) = \frac{1-(\tau^\infty/k)^2}{\tilde{r}(\eta)}-\frac{\tilde{r}(\eta)}{2}$$

$$g(\eta) = \tilde{r}(\eta)\cdot\left(\arctan\left(\frac{-(\tau^\infty/k)\sin 2\eta}{1-(\tau^\infty/k)\cos 2\eta}\right)+2\frac{\tau^\infty/k}{1-(\tau^\infty/k)^2}\sin 2\eta\right)$$

and θ_1, θ_2, are the roots of equations

$$\theta_1 = \theta-\ln\frac{c\tilde{r}(\theta_1)}{r},\quad \theta_2 = \theta+\ln\frac{c\tilde{r}(\theta_2)}{r}$$

However, solution (13), (14) is valid only for tensile loading when $\Delta P<0$ and $\xi=-1$.

3.2. Elastic Domain

[13] In the elastic zone we use the Kolossof-Muskhelishvili method for plane strain to obtain elastic fields given stress continuity on the unknown elastoplastic boundary L and far-field boundary conditions. We introduce the same complex variables z, $\bar{z}$ as before, centered at the origin of the hole. By applying the conformal mapping $z=w(\varsigma)$ to the z-plane, the elastic region is transformed onto the exterior of the unit circle γ in the complex ς-plane (Figure 2). Therefore, we introduce the additional unknown function $w(\varsigma)$ but the previously undetermined elastoplastic boundary becomes fixed. In other words, the unknown geometry is replaced by the unknown function. Now the stress components can be found from the formula

$$\sigma_{xx}+\sigma_{yy} = \sigma_{rr}+\sigma_{\theta\theta} = 4\mathrm{Re}\Phi(\varsigma)$$

$$\sigma_{yy}-\sigma_{xx}+2i\sigma_{xy} = (\sigma_{\theta\theta}-\sigma_{rr}+2i\sigma_{r\theta})e^{-2\theta i} = 2\left[\overline{w(\varsigma)}\frac{\Phi'(\varsigma)}{w'(\varsigma)}+\Psi(\varsigma)\right] \tag{15}$$

Omitting the mathematical details of the solution that can be found in the works by *Galin* [1946], *Kachanov* [1971], or *Chakrabarty* [2006] we write the final form of the functions appearing in (15):

$$\Phi(\varsigma) = -\frac{p+k\xi}{2}-k\xi\ln\frac{w(\varsigma)}{R\varsigma}$$

$$\Psi(\varsigma) = -\frac{k\xi}{\varsigma}\frac{\tilde{w}(\varsigma)}{w'(\varsigma)}$$

$$w(\varsigma) = c\left(\varsigma-\frac{\tau^\infty}{k\xi\varsigma}\right)$$

$$\tilde{w}(\varsigma) = c\left(\frac{1}{\varsigma}-\frac{\tau^\infty}{k\xi}\varsigma\right)$$

$$c = R\exp\left(\frac{\Delta P-k\xi}{2k\xi}\right) \tag{16}$$

The displacement field in the elastic zone is

$$2\mu(u_x + iu_y) = (3 - 4\nu)\varphi(\varsigma) - \frac{w(\varsigma)}{w'(\varsigma)}\overline{\varphi'(\varsigma)} - \overline{\psi(\varsigma)} \quad (17)$$

where

$$\varphi'(\varsigma) = \Phi(\varsigma)w'(\varsigma), \quad \psi'(\varsigma) = \Psi(\varsigma)w'(\varsigma)$$

$$\psi(\varsigma) = ck\xi\left(\frac{1}{\varsigma} + \frac{\tau^\infty}{k\xi}\varsigma\right)$$

$$\phi(\varsigma) = -k\xi w(\varsigma)\left(\ln\frac{w(\varsigma)}{R\varsigma} + \frac{p}{2k\xi} + \frac{1}{2}\right) - \frac{2c\tau^\infty}{\varsigma}$$

Displacement components u_x and u_y can be obtained from (17) as real and imaginary parts of the complex function on the right hand side. Figure 3 shows the maximum shear stress, the mean stress, and the elastic displacement field.

[14] The solution presented is applicable for compressible and incompressible materials. A compressible material is characterized by Poisson's ratio within the range $0 \le \nu < 0.5$ resulting in a finite bulk modulus. For an incompressible material, the Poisson's ratio is $\nu = 0.5$ and the bulk modulus is infinite. As can be seen from equation (11), the latter choice would lead to zero volumetric strain in the whole plate. Note that for incompressible materials with $\nu = 0.5$ both Tresca and von Mises yield criteria take the same form, and therefore the solution described in this section is equally valid for Tresca and von Mises types of plasticity.

[15] The analytical solution predicts an elliptical elastoplastic boundary with semi-axes $a = c(1 + |\tau^\infty/k|)$ and $b = c(1 - |\tau^\infty/k|)$. Its aspect ratio depends on the far-field shear stress τ^∞, and its area is controlled predominantly by the effective pressure ΔP. If $\sigma^\infty_{xx} = \sigma^\infty_{yy}$, i.e., there is a hydrostatic far-field stress state, the plastic zone will be a circle of radius c. As the far-field shear stress increases, the plastic zone elongates in the direction of far-field stress with the lesser absolute value, i.e., the plastic region is oriented horizontally when $|\sigma^\infty_{yy}| > |\sigma^\infty_{xx}|$ and vertically, vice versa. However, the analytical solution was obtained under certain assumptions of the nature of external loading and therefore the elliptic shape of the elastoplastic boundary as well as the analytical solution itself would be subject to some limitations that are discussed in section 3.3. Due to the correspondence principle this solution is valid for the viscoplastic materials if displacements in equation (17) are substituted with corresponding velocities.

3.3. Limits of Applicability of the Analytical Solution

[16] The derivation of the analytical solution required several assumptions about the nature of the external loads. These assumptions reduce the generality of the solution and produce its limitations. The first assumption is that the hole boundary needs to be enclosed in the elastoplastic boundary. Therefore, the length of the semi-axes of the elliptical plastic zone must satisfy the inequalities

$$a = c(1 + |\tau^\infty/k|) \ge R$$

$$b = c(1 - |\tau^\infty/k|) \ge R$$

Taking into account (16), the second, stronger inequality can be recast into

$$\exp\left(\frac{\Delta P - k\xi}{2k\xi}\right)(1 - |\tau^\infty/k|) \ge 1$$

which reduces to

$$\frac{\Delta P}{2k\xi} - \frac{1}{2} + \ln(1 - |\tau^\infty/k|) \ge 0 \quad (18)$$

[17] It is assumed that the problem is statically determined in the plastic region, which means that the stress field within the plastic zone does not "feel" the presence of the far-field loading and is influenced only by the pressure applied at the hole boundary. In other words, it is assumed that far-field shear stress does not disturb the axial symmetry of the stress field in the proximity of the hole. This is true only if every point in the plastic region can be connected to the hole rim by two slip-lines of different families lying entirely within the plastic domain or every slip-line cuts the elastoplastic boundary only once [*Hill*, 1950]. The slip-lines in the plastic zone are given by

$$\frac{dr}{d\theta} = \pm r \quad (19)$$

or

$$r \sim e^{\pm\theta} \quad (20)$$

The equation of the elastoplastic boundary in the ς-plane is $|\varsigma| = 1$, which can be rewritten through the polar coordinates (r,θ) in the physical plane as

$$r = c\frac{1 - (\tau^\infty/k)^2}{\sqrt{(\tau^\infty/k)^2 + 2(\tau^\infty/k\xi)\cos 2\theta + 1}} \quad (21)$$

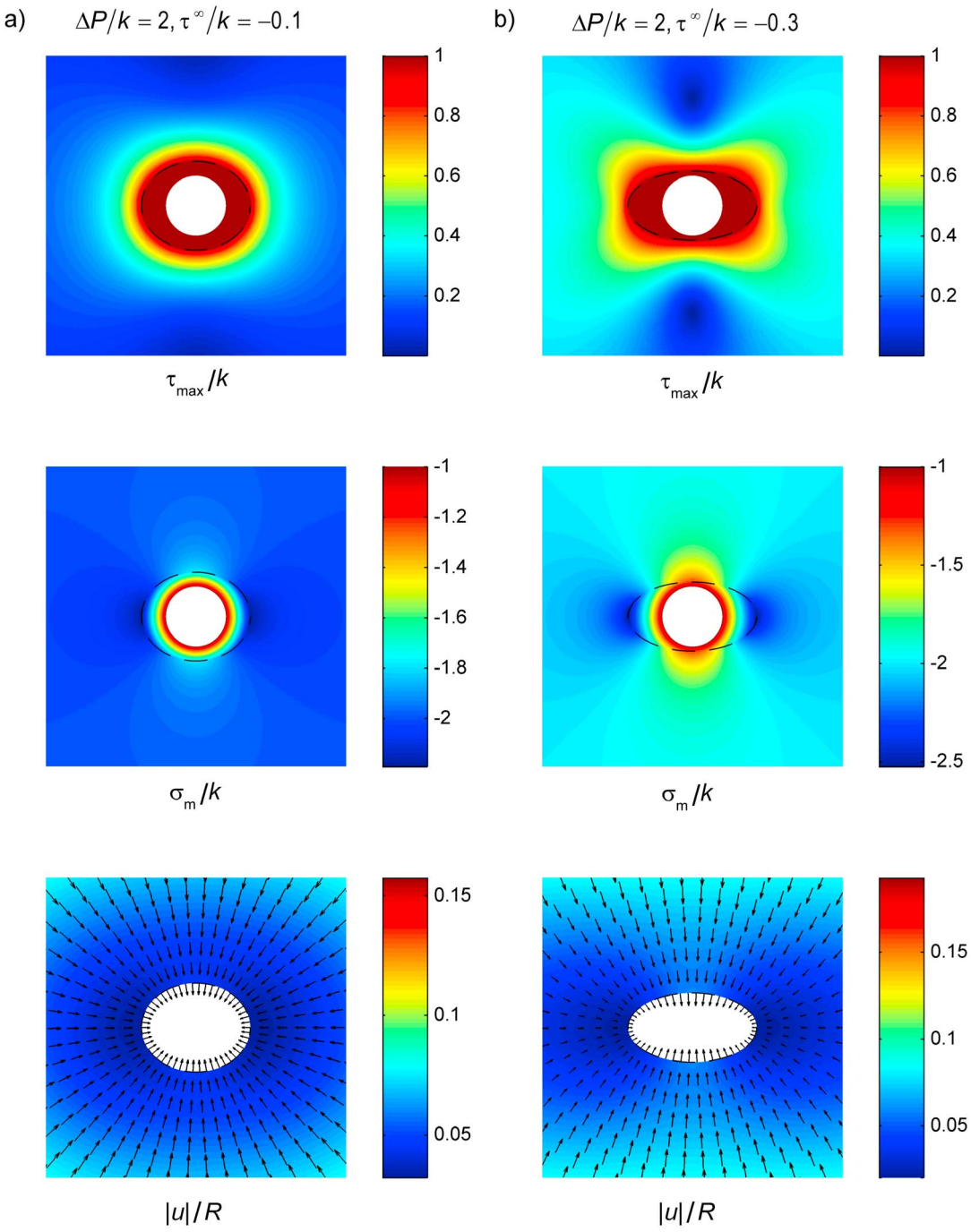

Figure 3. The maximum shear stress $\tau_{\max} = ((\sigma_{xx} - \sigma_{yy})^2/4 + \sigma_{xy}^2)^{1/2}$, the mean stress $\sigma_m = (\sigma_{xx} + \sigma_{yy})/2$ related to the yield limit k, and the absolute value of the displacement field $|u| = \sqrt{u_x^2 + u_y^2}$ related to the hole radius R. The plane is loaded by the combination of the far-field pressure $\Delta P/k = 2$ and different values of the far-field shear stress at zero inside pressure p. $E/k = 100$, $\nu = 0.3$. (a) $\tau^{\infty}/k = -0.1$ and (b) $\tau^{\infty}/k = -0.3$.

To find the intersection points of slip-lines and the elastoplastic boundary, we need to solve coupled nonlinear equations (20), (21) with respect to r and θ. Also, the slip-line and the boundary will have two intersection points at the very moment when the slip-line is tangent to the boundary (Figure 4). In this case tangents of two lines coincide with each other so the ellipse equation (21) also must satisfy differential

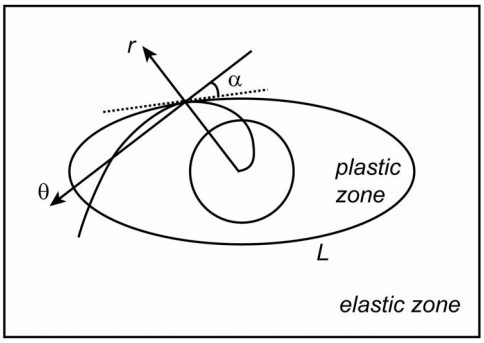

Figure 4. Limit of statical determinacy of the problem is given by the instant when one of the characteristic lines first touches the elastoplastic interface.

equations (19). Substitution of equation (21) into (19) leads to the following equation for θ

$$-2\sqrt{2}(\tau^{\infty}/k\xi)\cos(2\theta \pm \pi/4) = (\tau^{\infty}/k)^2 + 1$$

Since $|\cos(2\theta \pm \pi/4)| \leq 1$ the last equation has solutions only if

$$2\sqrt{2}|\tau^{\infty}/k| \geq (\tau^{\infty}/k)^2 + 1$$

This means that a slip-line would be tangent to the elastoplastic boundary only if $|\tau^{\infty}/k| \geq \sqrt{2} - 1$. Slip-lines that are tangent to the elastoplastic boundary at some point would necessarily intersect it at some other point (Figure 4) and therefore would touch the elastoplastic boundary twice. At lesser values of the shear stress all slip-lines will intersect the elastoplastic boundary once. Therefore a unique solution is only possible when

$$|\tau^{\infty}/k| < \sqrt{2} - 1 \tag{22}$$

The same inequality ensures that stresses in the elastic part of the plane do not exceed the yield limit. Inequality (22) limits the magnitude of the far-field shear stress beyond which plastic region is no longer elliptical.

[18] The next limitation comes from the assumption that $\sigma_{zz} = \nu(\sigma_{xx} + \sigma_{yy})$ is the intermediate stress. This assumption holds for an incompressible medium, but can be violated when $0 < \nu < 1/2$. For compressible media the inequality

$$-p - 2k\xi\ln(r/R) - k\xi + k \geq -2\nu(p + 2k\xi\ln(r/R) + k\xi)$$
$$\geq -p - 2k\xi\ln(r/R) - k\xi - k$$

must be fulfilled throughout the plastic region. This inequality provides us with the following limitations to the external loads:

$$-\frac{2(1-\nu)}{1-2\nu} \leq \frac{p\xi}{k} \leq \frac{2\nu}{1-2\nu}$$

$$\left|\frac{\Delta P}{k}\right| \leq -\frac{p\xi}{k} - 2\ln\left(1 + \left|\frac{\tau^{\infty}}{k}\right|\right) + \frac{1}{1-2\nu} \tag{23}$$

derived for minimum and maximum possible values of r.

[19] The analytical solution does not encompass unloading and every subsequent change of external loads leads to further loading. Therefore, the plastic zone can only grow or at least stay unchanged, i.e., increments of elastoplastic interface semi-axis da and db must be nonnegative:

$$da = dc(1 + |\tau^{\infty}/k|) + c\,d|\tau^{\infty}/k| \geq 0$$

$$db = dc(1 - |\tau^{\infty}/k|) - c\,d|\tau^{\infty}/k| \geq 0$$

With (16) this leads to the following limitation on the increments of external loads:

$$|d(\Delta P)/k| \geq \frac{2|d\tau^{\infty}/k|}{1 - |\tau^{\infty}/k|} \tag{24}$$

Figure 5 illustrates the range of admissible parameters for the analytical solution. If the stress state plots within Region 1, then the method described in this chapter can be used. Region 3 corresponds to the pure elastic state, where Kolossof-Muskhelishvili's method gives the solution. If the stress point is close to the boundary between Regions 2 and 3, the *Bykovtsev and Tsvetkov*'s [1987] approximate solution can be used. In general, Region 2 corresponds to the onset of yielding, where several separate plastic regions appear around the hole. Region 4 corresponds to the more evolved plastic zone with several separate domains of plastic flow, which can leave some parts of the hole boundary in the elastic state. In Region 5 the plastic domain covers the hole rim entirely, but it is no longer an ellipse and the additional "wings" start to grow in four diametrically opposite directions. Regions 1–5 correspond to the same edge of the Tresca yield surface with σ_{zz} as an intermediate stress. On the other hand, if the stress point lies within Zone 6, σ_{zz} is no longer an intermediate stress and other edges of the Tresca prism must be considered. The position of the line bounding Zone 6 depends on Poisson's ratio, shifting left for soft materials and right for stiff materials. For incompressible materials

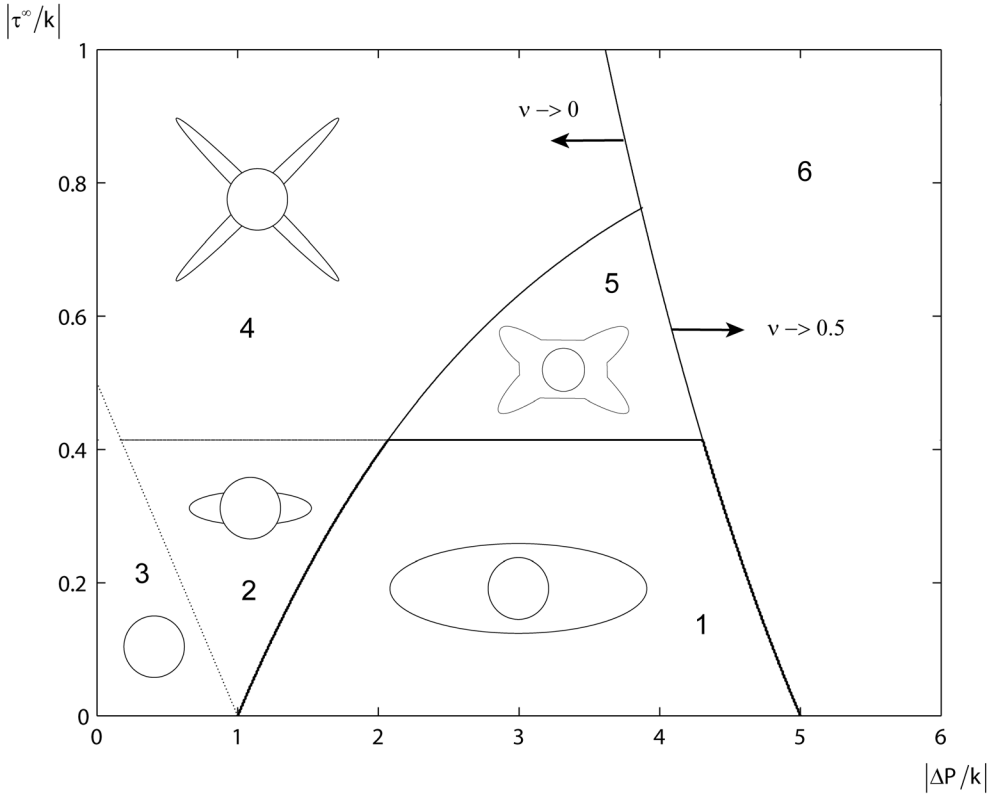

Figure 5. The permissible range of loading parameters for the applicability of Galin's solution lies in Zone 1. Zone 3 represents a purely elastic state. If the stress state lies in Zones 2, 4, 5 or 6, then a numerical modeling is needed. Within Zone 6, σ_z is no longer an intermediate stress. The position of the line bounding Zone 6 depends on Poisson's ratio, shifting right with increasing ν and left with decreasing. The position of the line corresponds to $\nu = 0.4$.

this line shifts to infinity, so that Galin's analytical solution does not have limitations on the effective pressure magnitude. The uppermost line $|\tau^{\infty}|/k = 1$ gives the fully plastic state in the body. Note that if the stresses lie in Regions 2, 4, 5, or 6, then a numerical modeling will have to be used to investigate deformation around the hole.

4. Numerical Stress Integration

4.1. Forward Euler Algorithm and Continuum Tangent Modular Matrix

[20] For very small load increments, we could integrate (7) using (8) and replacing $\dot{e}$ with Δe. However, the strain and subsequent stress changes are not infinitesimally small and, as a consequence, errors accumulate. For a numerical implementation equations (1)–(8) need to be modified. For plane strain the nonzero strain components may be listed in the column vector

$$\mathbf{e} = [\, e_{xx} \quad e_{yy} \quad 2e_{xy} \,]^T$$

The in-plane stresses are written as

$$\boldsymbol{\sigma} = [\, \sigma_{xx} \quad \sigma_{yy} \quad \sigma_{xy} \,]^T$$

The stress normal to the xy plane may be evaluated as

$$\sigma_{zz} = \nu(\sigma_{xx} + \sigma_{yy})$$

We assume that at time t all the quantities are known and their new values at time $t + dt$ need to be updated. Hooke's law (4) may be rewritten as

$$\dot{\boldsymbol{\sigma}} = D\dot{\mathbf{e}}^e = D(\dot{\mathbf{e}} - \dot{\mathbf{e}}^p) \tag{25}$$

where the constitutive matrix D for plane strain has a form

$$D = \frac{E}{(1+\nu)(1-2\nu)} \begin{pmatrix} 1-\nu & \nu & 0 \\ \nu & 1-\nu & 0 \\ 0 & 0 & (1-2\nu)/2 \end{pmatrix} \tag{26}$$

The flow rule can be represented as

$$\dot{\mathbf{e}}^p = \dot{\lambda}\frac{\partial Q}{\partial \boldsymbol{\sigma}} \tag{27}$$

Integration of the flow rule equation (27) according to the forward Euler algorithm implies that $\partial Q/\partial \boldsymbol{\sigma}$ is calculated at time t and therefore is the known quantity. The algorithmic counterpart of equation (27) can be written as

$$\dot{\mathbf{e}}^{p}_{t+dt} = \dot{\lambda}_{t+dt} \left.\frac{\partial Q}{\partial \boldsymbol{\sigma}}\right|_{t} \tag{28}$$

Below we follow the general procedure for deriving a complete stress-strain relationship in the rate form, based on the consistency condition, which assumes that during loading the old and new stress states are both on the yield surface [*Prager*, 1949], i.e., $dF = F_{t+dt} - F_t = 0$. But in numerical calculations one has only approximate fulfillment of the yield criterion, i.e., a systematic drift from the yield surface, until special measures are taken to return stresses to the yield surface. This drift has no physical meaning and is insignificant so that quite often incremental algorithms ignore it [*Crisfield*, 1991]. However, it influences the accuracy of the solution. If special measures for returning stresses to the yield surface are not taken, one needs to formulate a numerical consistency condition which accepts the fact that the old stress state can deviate from the yield surface in order to minimize the drift and to demand fulfillment of a yield criterion only from the new stresses ($F_{t+dt} = 0$). In this way, a linearization of the yield function around the previous stress state corresponding to instant t with yield function F_t gives

$$F_{t+dt} = F_t + \frac{\partial F}{\partial \boldsymbol{\sigma}} \dot{\boldsymbol{\sigma}}\, dt \tag{29}$$

where $\partial F/\partial \boldsymbol{\sigma}$ is a three component row vector, calculated at time t, and $F_t \neq 0$. Substitution of equation (25) into (29) and subsequent use of the numerical consistency condition together with the plastic flow rule leads to

$$F_{t+dt} = F_t + \frac{\partial F}{\partial \boldsymbol{\sigma}} D \left(\dot{\mathbf{e}} - \dot{\lambda} \frac{\partial Q}{\partial \boldsymbol{\sigma}} \right) dt = 0$$

where $\partial Q/\partial \boldsymbol{\sigma}$ is a column vector of three components. From the last equation we obtain

$$\dot{\lambda} = \frac{\dfrac{\partial F}{\partial \boldsymbol{\sigma}} D\, \dot{\mathbf{e}}}{\dfrac{\partial F}{\partial \boldsymbol{\sigma}} D \dfrac{\partial Q}{\partial \boldsymbol{\sigma}}} + \frac{F_t}{\dfrac{\partial F}{\partial \boldsymbol{\sigma}} D \dfrac{\partial Q}{\partial \boldsymbol{\sigma}} dt} \tag{30}$$

Substituting plastic strain rates (28) together with $\dot{\lambda}$ taken in the form (30) into equation (25) we obtain the final form of the elastoplastic stress-strain relationship

$$\dot{\boldsymbol{\sigma}} = D^{ep}\, \dot{\mathbf{e}} - \frac{dF_{correction}}{dt} \tag{31}$$

Here, we introduced the elastoplastic tangent modular matrix, an algorithmic counterpart of the continuum matrix (8), and the new column vector quantity according to

$$D^{ep} = D \left(I - \frac{\dfrac{\partial Q}{\partial \boldsymbol{\sigma}} \dfrac{\partial F}{\partial \boldsymbol{\sigma}} D}{\dfrac{\partial F}{\partial \boldsymbol{\sigma}} D \dfrac{\partial Q}{\partial \boldsymbol{\sigma}}} \right) \tag{32}$$

$$dF_{correction} = \frac{F_t D \dfrac{\partial Q}{\partial \boldsymbol{\sigma}}}{\dfrac{\partial F}{\partial \boldsymbol{\sigma}} D \dfrac{\partial Q}{\partial \boldsymbol{\sigma}}} \tag{33}$$

I is the 3 × 3 identity matrix. Comparing equation (31) with the analytical stress-strain relation (7) one can see that there is an additional term in (31) that corrects the drift from the yield surface due to numerical inaccuracy. Previously, drift from the yield surface within the incremental integration procedure was discussed by *Zhao et al.* [2005].

[21] The first numerical approach under analysis is based on the incremental first-order forward Euler solution strategy with correction of the drift from the yield surface and use of continuum tangent moduli (32). The load is applied incrementally until the final value is reached. At every stepwise application of the external load, the trial stresses are calculated according to elastic Hooke's law. Then, the trial yield function is calculated and if it does not exceed zero, elastic calculations are performed. If it exceeds zero, then plasticity calculations are initiated based on the current values of stresses, which are below or on the yield surface. The algorithm is combined with Galerkin's finite element method in its weak form and implemented in MATLAB. A flow diagram of the computer code is presented in Figure 6.

4.2. Backward Euler Algorithm and Consistent Tangent Modular Matrix

[22] Employing the backward Euler algorithm to integration of the flow rule (27) yields

$$\dot{\mathbf{e}}^{p}_{t+dt} = \dot{\lambda}_{t+dt} \left.\frac{\partial Q}{\partial \boldsymbol{\sigma}}\right|_{t+dt}$$

Unlike the forward Euler scheme, new plastic strain increments are updated by new and yet unknown values of $\partial Q/\partial \boldsymbol{\sigma}$. In order to find them the linearization is applied:

$$\left.\frac{\partial Q}{\partial \boldsymbol{\sigma}}\right|_{t+dt} = \left.\frac{\partial Q}{\partial \boldsymbol{\sigma}}\right|_{t} + \left.\frac{\partial^2 Q}{\partial \boldsymbol{\sigma}^2}\right|_{t} \dot{\boldsymbol{\sigma}}\, dt$$

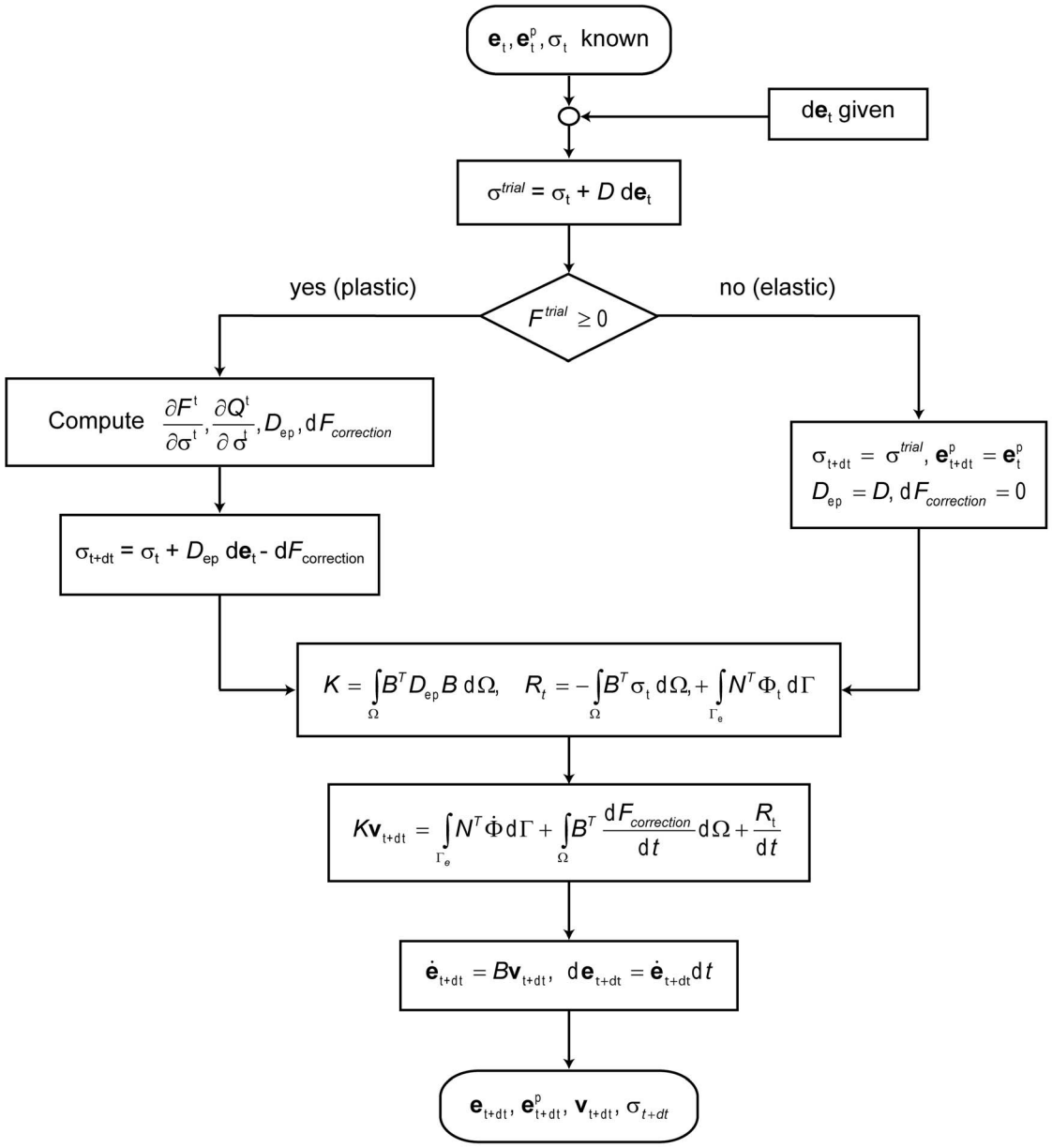

Figure 6. Flow diagram of forward Euler algorithm for one time step iteration. **N** is the shape functions vector, **Φ** is the given traction value on the essential volume boundary Γ_e and B is the usual small strain matrix. R_t is the unbalanced force vector (or residual). Adding it to the applied loads improves the accuracy of the simple forward Euler scheme.

where $\partial^2 Q/\partial \boldsymbol{\sigma}^2$ is 3×3 matrix of second derivatives. Substituting the last two equations into Hooke's law (25) leads to

$$\dot{\boldsymbol{\sigma}} = D\dot{\mathbf{e}} - D\dot{\lambda}\left(\frac{\partial Q}{\partial \boldsymbol{\sigma}} + \frac{\partial^2 Q}{\partial \boldsymbol{\sigma}^2}\dot{\boldsymbol{\sigma}}\, dt\right)$$

Here and again later, we omitted a subscript referring to step $t + dt$. Solving this equation for $\dot{\boldsymbol{\sigma}}$ we obtain

$$\dot{\boldsymbol{\sigma}} = \left(I + D\, d\lambda \frac{\partial^2 Q}{\partial \boldsymbol{\sigma}^2}\right)^{-1} D\left(\dot{\mathbf{e}} - \dot{\lambda}\frac{\partial Q}{\partial \boldsymbol{\sigma}}\right) = PD\left(\dot{\mathbf{e}} - \dot{\lambda}\frac{\partial Q}{\partial \boldsymbol{\sigma}}\right) \tag{34}$$

Normally, the backward Euler algorithm is combined with procedures that ensure that stresses lie exactly on the yield surface with help of one of the return mapping algorithms [*Crisfield*, 1991; *Simo and Hughes*, 1998; *Simo*, 1998]. These algorithms give the necessary value of plastic multiplier increment $d\lambda$, guaranteeing the exact fulfillment of yield criterion. However, the rate of the plastic multiplier is still unknown. In order to find it we substitute (34) into consistency condition $F_{t+dt} = 0$ together with (29), where $F_t = 0$, obtaining

$$\frac{\partial F}{\partial \boldsymbol{\sigma}} PD\left(\dot{\mathbf{e}} - \dot{\lambda}\frac{\partial Q}{\partial \boldsymbol{\sigma}}\right) dt = 0$$

The solution of last equation gives

$$\dot{\lambda} = \frac{\frac{\partial F}{\partial \boldsymbol{\sigma}} PD\dot{\mathbf{e}}}{\frac{\partial F}{\partial \boldsymbol{\sigma}} PD\frac{\partial Q}{\partial \boldsymbol{\sigma}}}$$

Substituting this result back into (34) we obtain

$$\dot{\boldsymbol{\sigma}} = D^{ep}\dot{\mathbf{e}} \tag{35}$$

where

$$D^{ep} = PD\left(I - \frac{\frac{\partial Q}{\partial \boldsymbol{\sigma}}\frac{\partial F}{\partial \boldsymbol{\sigma}} PD}{\frac{\partial F}{\partial \boldsymbol{\sigma}} PD\frac{\partial Q}{\partial \boldsymbol{\sigma}}}\right) \tag{36}$$

and

$$P = \left(I + D\,d\lambda\frac{\partial^2 Q}{\partial \boldsymbol{\sigma}^2}\right)^{-1} \tag{37}$$

[23] The description of this algorithm and its flowcharts is given by *Simo and Hughes* [1998]. The external load is applied in several increments until the final value is reached. Within every increment an iterative procedure is used for solution of nonlinear constitutive equations. Here, we use the Picard iteration method and the Newton-Raphson iterative method employing consistent tangent and continuum tangent modular matrices. It guarantees that both mechanical equilibrium and the yield criterion are satisfied. Also, the design of the algorithm precludes recording the transient loading/unloading stages in the solution vector at the end of iterations.

5. Benchmarking Strategy and Results

[24] The accuracy of the numerical solutions obtained using forward and backward Euler integration is verified against Galin's analytical solution. The stress equilibrium equations were solved using self-developed finite element codes implemented in MATLAB. We employed a four-noded isoparametric quadrilateral element in the code implementing the forward Euler method. The backward Euler code utilizes unstructured triangular computational meshes and builds upon finite element solver MILAMIN [*Dabrowski et al.*, 2008]. In both cases the computational mesh was refined in the vicinity of the hole. For the benchmarking purposes, we used the associated plasticity model

$$F = Q = (\sigma_{xx} - \sigma_{yy})^2/4 + \sigma_{xy}^2 - k^2 \tag{38}$$

Computations were performed for compressible and incompressible solids. However, it must be remembered that for compressible materials ($0 \le \nu < 0.5$) equation (38) represents only one edge of Tresca prism on which σ_{zz} is an intermediate principal stress and therefore, requirement (23) is fulfilled.

[25] The increments of tractions are prescribed on the outer boundary. The hole rim is stress-free. We load the system from the stress-free initial configuration until the mean stress on the outer rim $-(\sigma_{xx}^{out} + \sigma_{yy}^{out})/2$ reaches given value P^{∞}. The shear stress on the external radius $\tau^{out} = ((\sigma_{xx}^{out} - \sigma_{yy}^{out})^2/4 + (\sigma_{xy}^{out})^2)^{1/2}$ increases during loading while the condition (22) is fulfilled and then remains on the same level. The increments of the boundary tractions satisfy (24). After the mean stress on the external boundary reaches a certain threshold, it is used together with the current value of the far-field shear stress to find $\tau_{\max} = ((\sigma_{xx} - \sigma_{yy})^2/4 + \sigma_{xy}^2)^{1/2}$ and the mean stress $\sigma_m = (\sigma_{xx} + \sigma_{yy})/2$ according to analytical equations (10)–(16). The maximum value of effective pressure reached corresponds to the upper boundary of applicability of the analytical solution.

[26] In our tests of the forward Euler method, the mean and maximum shear stresses in the midpoint of elements are compared to the analytical results. The numerical grid corresponds to the analytical z-plane (Figure 2). Note that the plastic stress field (10) is calculated by means of the space variables of z-plane, while the equations (15) and (16) for elastic stresses operate with ς-plane. To be able to use the same numerical grid in both elastic and plastic regions one needs first to relate two complex variables as

$$\varsigma = \frac{z}{2c} + \frac{\sqrt{z^2 + 4\xi c^2\tau^{\infty}/k}}{2\xi c} \tag{39}$$

in the first quadrant of the z-plane, where z can be constructed from Cartesian coordinates x, y of the

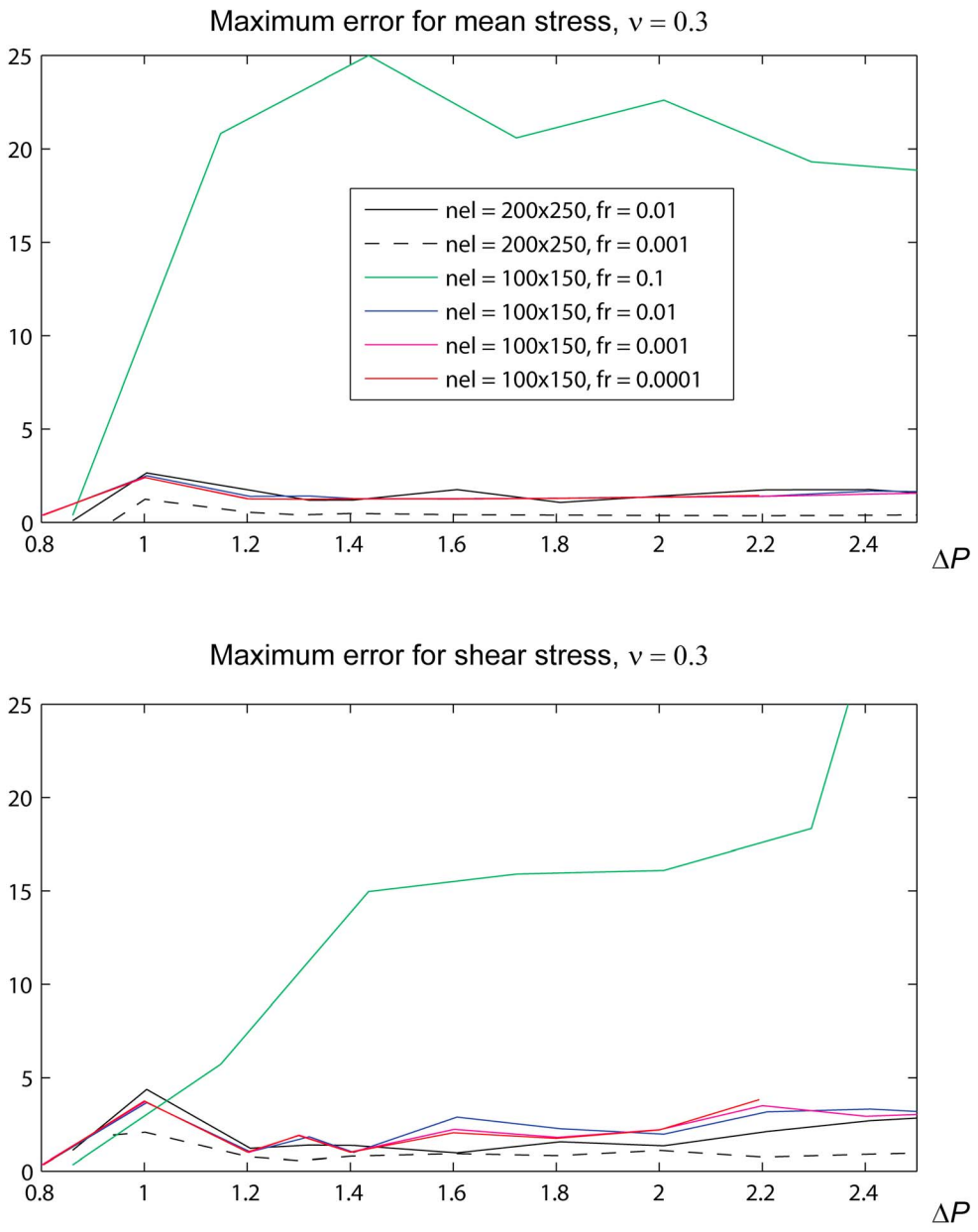

Figure 7. The accuracy of the incremental algorithm as a function of spatial resolution and a number of increments calculated for Poisson ratio 0.3. The curves correspond to a different number of elements *nel*, and different time increments are defined by a value of multiplier *fr* in equation (40). The plots show that time step is a main factor influencing accuracy. For big time steps the numerical solution diverges from the exact result significantly. However, if $fr \leq 0.01$, the accuracy is nearly identical for various values of *fr* and depends mostly on spatial resolution.

numerical grid points as $z = x + iy$. Since the forward Euler method does not employ any iterative procedure within one time step, the right choice of the time increment dt is crucial. We force

$$dt = fr \min_{\Omega} \sqrt{x^2 + y^2} \Big/ \max_{\Omega}(|v_x|, |v_y|) \qquad (40)$$

where *fr* is the constant multiplier.

[27] The percentage error, for both mean and maximum shear stresses, is defined as the absolute value of the difference between the analytical and numerical solutions normalized by the maximum absolute value of the analytical solution in the domain:

$$Err(x,y) = \frac{|g^{an}(x,y) - g^{nu}(x,y)|}{\max\limits_{\Omega} |g^{an}(x,y)|} \cdot 100\% \qquad (41)$$

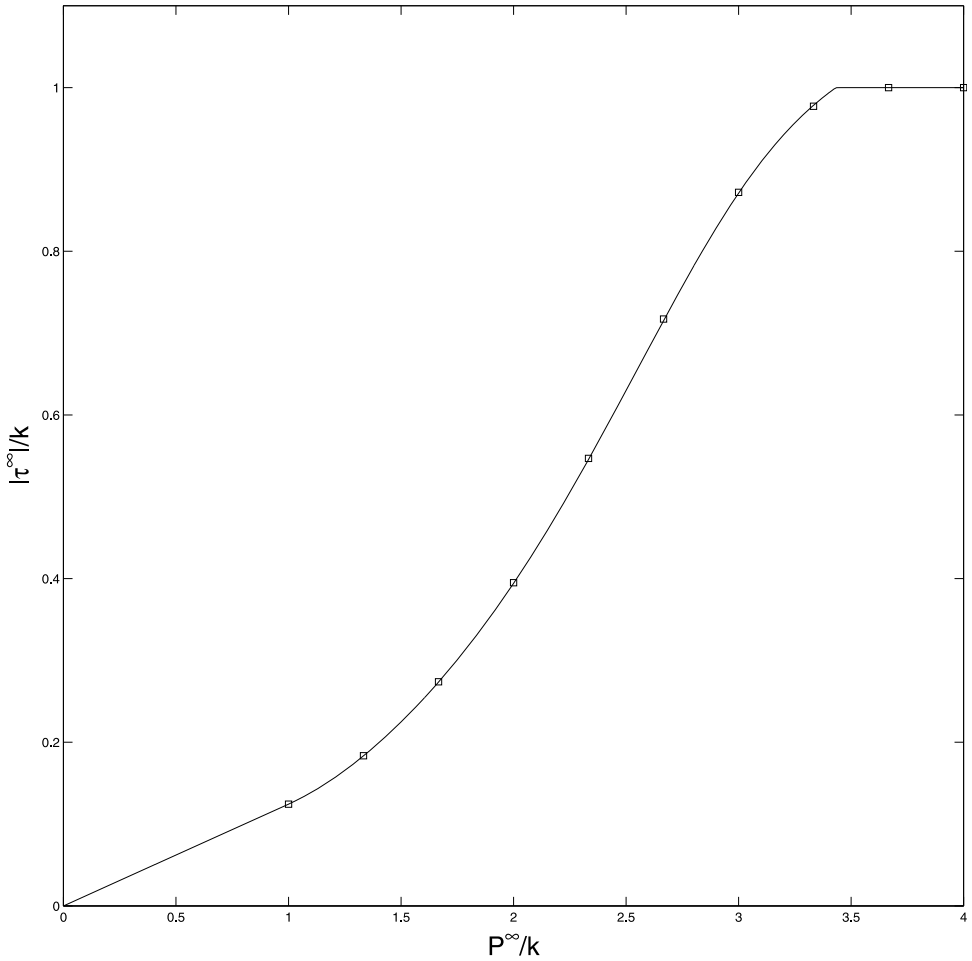

Figure 8. The second invariant of deviatoric stress tensor as a function of the effective pressure. Both measures are normalized by the yield strength. The Poisson ratio was set to 0.5 in the model. The model is loaded exclusively by pressure up to $P^{\infty}/k = 1$. Later, linear increments of shear stress at the external boundary accompanied the pressure load. The ratio of pressure increment to shear stress increment was kept constant and equal to $\sqrt{2}$ in order to fulfill requirement (24). The loading path is shown in a single point located at $x = 2$, $y = 2$. The solid line corresponds to the analytical result. The square markers stand for numerical results obtained using the consistent tangent approach. The horizontal distance between the numerical data reflects actual pressure increments used in the simulation. Spatial resolution corresponds to 100,000 nodes.

where $g^{an}(x,y)$ and $g^{nu}(x,y)$ are the analytical and numerical values of the function in question, respectively. Figure 7 shows the error for different space resolutions and time steps with various values of *fr*. Figure 7 shows that $fr = 0.01$ already gives acceptable values of the error; further decreasing *dt* only slightly improves it, indicating that the error is mostly controlled by the resolution. Using $fr > 0.01$ results in the introduction of a significant error related to the stress integration.

[28] Figure 8 shows the loading curve in a selected point in one of the tests employing the backward Euler method. The stress build-up is reproduced with a high accuracy even though load increments were large (only ~10 steps to reach the maximum load). Figure 9 shows the convergence of the residual for a selected load increment. The results obtained using the Picard iteration method and the Newton-Raphson iteration method employing continuum and consistent tangent matrices are presented. The Picard iterations are characterized by the slow monotonic convergence. The Newton-Raphson iterations, particularly if the consistent tangent matrix is used, exhibit an abrupt convergence of the residual toward the machine precision. However, the latter method is prone to divergence problems, especially at the initial stage of iterations, when the number of integration points with the shear stress exceeding the yield strength oscillates. To circum-

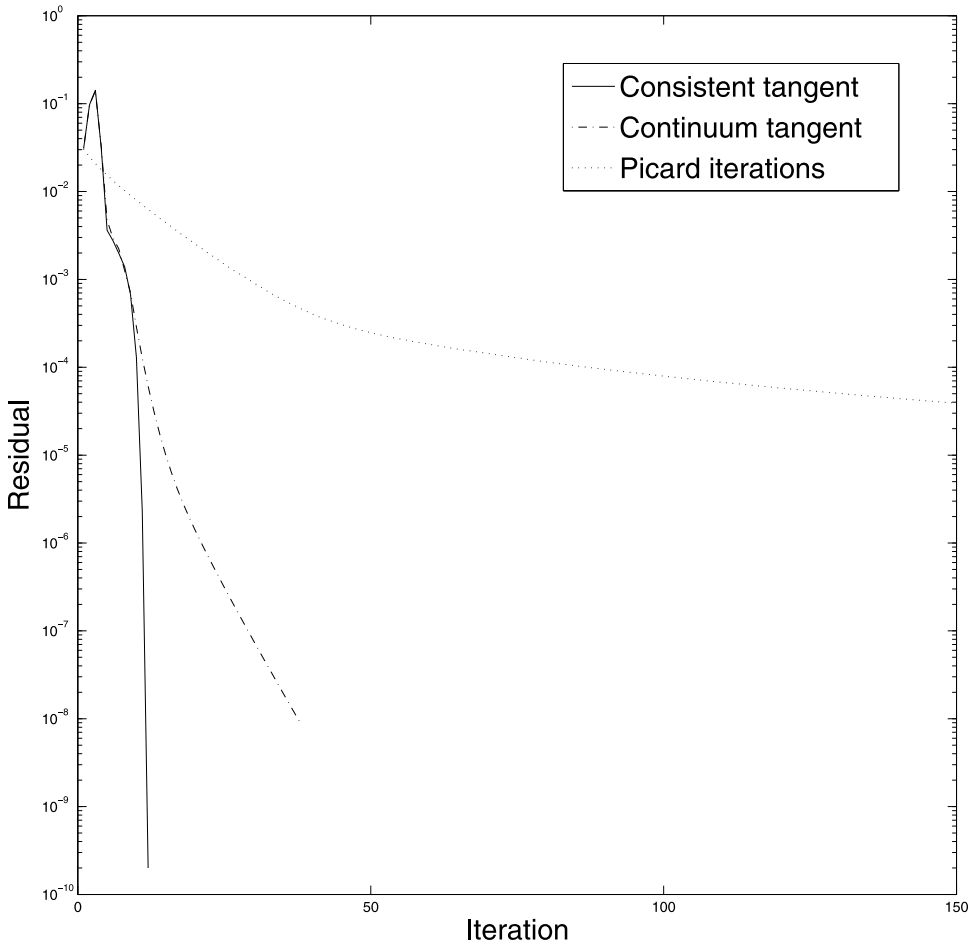

Figure 9. The convergence of the L_2 norm of the unbalanced force vector (or residual) for the consistent tangent, continuum tangent and Picard iterations. The results are shown for the seventh load increment. The machine precision was reached in the consistent tangent approach after approximately 10 iterations.

vent this problem we suggest using the Picard iteration method initially and switching to the Newton-Raphson iterations afterward in addition to employing standard techniques such as the line search to improve the convergence radius.

6. Conclusions

[29] In this paper we offer a two-dimensional analytical benchmark with combined pressure and shear loading for elastoplastic and viscoplastic numerical models. The benchmark is based on an elastoplastic analytical solution for non-isotropic contraction (expansion) of an infinite plate with a circular hole under plane strain or plain stress conditions. The viscoplastic solution follows from the elastoplastic solution due to the correspondence principle. We discuss the benchmark strategy and boundaries of applicability of the analytical solution. This paper presents our implementation of four MATLAB-based finite element elastoplastic solvers. The first is based on a forward Euler algorithm with a continuum tangent modular matrix. Two other codes represent a realization of a modified Newton-Raphson algorithm with consistent and continuum tangent modular matrixes. Picard iterations are implemented in the fourth solver. For an incremental forward Euler algorithm we show how the accuracy of the numerical solution depends on the time step. For iterative algorithms we show that very accurate numerical results can be obtained if convergence is guaranteed.

Acknowledgments

[30] We are grateful to Ritske Huismans, Harro Schmeling, and an anonymous reviewer whose constructive comments have improved this paper. This study was supported by the Norwegian

Research Council under an Outstanding Young Investigators grant and a Center of Excellence grant.

References

Barthold, F.-J., M. Schmidt, and E. Stein (1998), Error indicators and mesh refinements for finite-element-computations of elastoplastic deformations, *Comput. Mech.*, *22*, 225–238.

Bykovtsev, G. I., and Y. D. Tsvetkov (1987), Two-dimensional problem of the loading of an elastoplastic plane weakened by a hole, *J. Appl. Math. Mech.*, *51*(2), 244–250(PMM), doi:10.1016/0021-8928(87)90071-2.

Chakrabarty, J. (2006), *Theory of Plasticity*, Elsevier, Amsterdam.

Crisfield, M. A. (1991), *Non-linear Finite Element Analysis of Solids and Structure*, vol. I, John Wiley, Chichester, U. K.

Dabrowski, M., M. Krotkiewski, and D. W. Schmid (2008), MILAMIN: MATLAB-based finite element method solver for large problems, *Geochem. Geophys. Geosyst.*, *9*, Q04030, doi:10.1029/2007GC001719.

Davis, R. O., and A. P. S. Selvadurai (2002), *Plasticity and Geomechanics*, doi:10.1017/CBO9780511614958, Cambridge Univ. Press, Cambridge, U. K.

Galin, L. A. (1946), Plane elastoplastic problem, *Prikl. Mat. Mekh.*, *10*, 367–386.

Hill, R. (1950), *The Mathematical Theory of Plasticity*, Clarendon, Oxford, U. K.

Ivlev, D. D. (1957), On the determination of displacements in Galin's problem, *Prikl. Mat. Mekh.*, *21*(5), 716–717.

Kachanov, L. M. (1971), *Foundations of the Theory of Plasticity*, North-Holland, Amsterdam.

Krabbenhoft, K., A. V. Lyamin, S. W. Sloan, and P. Wriggers (2007), An interior-point algorithm for elastoplasticity, *Int. J. Numer. Methods Eng.*, *69*, 592–626.

Krieg, R. D., and D. B. Krieg (1977), Accuracies of numerical solution methods for the elastic-perfectly plastic model, *J. Pressure Vessel Technol.*, *99*, 510–515.

Muskhelishvili, N. I. (1953), *Some Basic Problems of the Mathematical Theory of Elasticity*, Noordhoff, Groningen, Netherlands.

Ortiz, M., and E. P. Popov (1985), Accuracy and stability of integration algorithms for elastoplastic constitutive relations, *Int. J. Numer. Methods Eng.*, *21*(9), 1561–1576, doi:10.1002/nme.1620210902.

Ostrosablin, N. I. (1984), *Plane Elastoplastic Distribution of Stresses Near Round Holes* (in Russian), Nauka, Novosibirsk, Russia.

Prager, W. (1949), Recent developments in the mathematical theory of plasticity, *J. Appl. Phys.*, *20*, 235–241, doi:10.1063/1.1698348.

Roberts, S. M., F. R. Hall, A. Van Bael, P. Hartley, I. Pillinger, C. E. N. Sturgess, P. Van Houtte, and E. Aernoudt (1992), Benchmark tests for 3-D, elasto-plastic, finite-element codes for the modeling of metal forming processes, *J. Mater. Processing Technol.*, *34*, 61–68, doi:10.1016/0924-0136(92)90090-F.

Rudnicki, J. W., and J. R. Rice (1975), Conditions for the localization of deformation in pressure-sensitive dilatant materials, *J. Mech. Phys. Solids*, *23*, 371–394, doi:10.1016/0022-5096(75)90001-0.

Simo, J. C. (1998), Numerical analysis and simulation of plasticity, in *Handbook of Numerical Analysis*, vol. 6, edited by P. G. Ciarlet and J. L. Lions, pp. 183–499, Elsevier, Netherlands.

Simo, J. C., and T. J. R. Hughes (1998), *Computational Inelasticity*, Springer, New York.

Wieners, C. (1999), Multigrid methods for Prandtl-Reuss plasticity, *Numer. Linear Algebra Appl.*, *6*, 457–478, doi:10.1002/(SICI)1099-1506(199909)6:6<457::AID-NLA173>3.0.CO;2-P.

Yu, H.-S. (2006), *Plasticity and Geotechnics*, Springer, New York.

Zhao, J., D. Sheng, M. Rouainia, and S. W. Sloan (2005), Explicit stress integration of complex soil models, *Int. J. Numer. Anal. Methods Geomech.*, *29*, 1209–1229, doi:10.1002/nag.456.